THE UNIVERSITY *of* EDINBURGH
School of Physics and Astronomy

Senior Honours Project
Modelling Observations of Eccentric Circumbinary Discs

Aidan D. Johnson
31 March, 2023

Abstract

Protoplanetary discs have been observed to exhibit structures that are not entirely flat. Warps can arise in their outer discs and detached, misaligned inner discs may develop, which are responsible for creating shadowing effects extending across entire discs. Prior research linked many of these discs to possessing a central host binary pair. Simulations of circumbinary discs varying solely in host star eccentricity were performed in order to understand the link between host star eccentricity and disc morphology. Eccentricities up to 0.6 may produce minor warping in their outer discs, and an eccentricity of 0.8 produces a detached inner disc, rotating independently of its outer disc. This inner disc misalignment induces fluctuations in luminosity and shadow orientation, which could both be observed in nature, and could lead to a potential explanation for dipper stars. It was also found that the outer disc shadow angles can be calculated for these high eccentricity scenarios.

Declaration

I declare that this project and report is my own work.

Supervisors: Dr. Alison K. Young and Professor Ken Rice   10 Weeks

Contents

1   Introduction

Since the first observation of a protoplanetary disc using the Hubble telescope in 1994, studies into planet formation have developed significantly (O'dell and Wen, 1994). Major developments in instrumentation and observational techniques, alongside substantial improvements in computing simulations means that we are now learning more about planet formation than ever before. This paper uses simulations of protoplanetary discs to understand the ways in which they can warp and deform in the presence of binary hosts (circumbinary discs), and specifically focuses on how their host star's eccentricities can induce these deformations. The ways in which their shadows evolve is also analysed and it is seen if these are indicative of warping or a detached inner disc.

2   Background

2.1   Motivations for study

One of the earliest stages in planet formation is the protoplanetary disc. These arise from the collapse of giant molecular clouds - our solar system's cloud estimated at having been ≈ 20 parsecs in diameter (Montmerle et al., 2006). This gradually collapses due to its own gravity, forming a central protostar (that will eventually spark fusion, if its mass allows) with a protoplanetary disc surrounding it (Armitage, 2010). Our knowledge of the chemical processes within protoplanetary discs has improved significantly from observations made via the Atacama Large Millimetre Array (ALMA), due

to its improved sensitivity and spatial resolution. A depiction of the physical processes that occur within a disc can be viewed in Figure 1.

Conservation of angular momentum allows the initially spherical cloud to collapse to form a relatively thin, rotationally-supported circumstellar disc. Planet formation in the disc can then lead to all planets orbiting in the same plane - as is the case within our own solar system. Although this is typically the case, recent research has shown these protoplanetary discs often become misaligned, warped and deformed. This could supply us with an explanation for formation of planets in retrograde or oblique orbits, which make up $\approx 40\%$ of short-period exoplanets (Kraus et al., 2020). These warps are not always unstable, as one would initially believe. Conditions for the formation of stable warps in circumbinary discs will be a primary focus of this paper, alongside whether observations of these effects in nature are viable.

2.2   A summary of recent research

The first work to look in detail at disc misalignments was carried out in the 1990s, and gained significant momentum in the 2010s, with the main focus initially being on binary Super Massive Black-hole (SMBH) systems, alongside binaries formed from stars in a cluster (C. J. Nixon et al., 2011). SMBH's in high accretion states are observed to have thin and viscous accretion discs - much different to significantly thicker protoplanetary discs. It was originally believed that due to their thickness and low
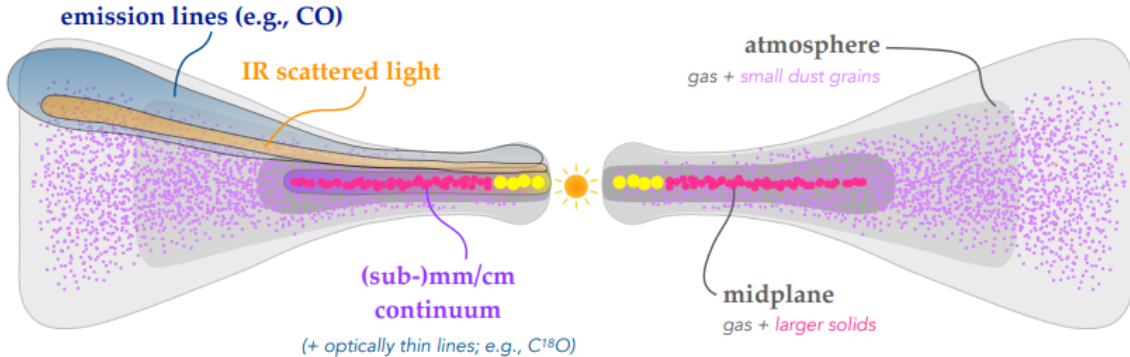
Figure 1: Cross-section depicting the inner-compositon of a protoplanetary disc, from the central host star to the outer disc edge, taken from Andrews (2020). The gas is denoted in grey, the solids marked with colours - figure is *not* to scale. Both the vertical component of stellar gravity and the vertical pressure gradient forces balance out, maintaining the disc's flat structure (Walsh et al., 2010; Cleeves, 2017). Magnetised winds are also present along the flat surfaces of these discs, which are believed to be the primary mechanisms inducing accretion (Lesur, Geoffroy R. J., 2021). The disc is also subject to external UV radiation, which is proposed to be the dominant environmental influence in protoplanetary discs (Winter and Haworth, 2022).

viscosity their warps were thought to dissipate throughout the disc, maintaining their flat structure, but this is not the case.

Further research into specifically misaligned circumbinary discs was carried out in 2013, unveiling a variety of information about disc warps and misalignments. The geometry of a misaligned inner disc can be viewed in Figure 2. Tearing was discovered to be common, which increases the accretion rate, accelerating the disc's evolution and losing angular momentum (C. Nixon et al., 2013). Disc tearing can allow gases in the disc to bypass the angular momentum barrier to accretion, instead of relying on viscously-driven angular momentum transport. Currently, no correlation between disc properties and the radius of inner disc tearing has been observed. Circumbinary discs are prone to breaking at almost all inclinations, which has multiple causes, such as an eccentric host binary, from gravitational interactions with highly massive companions or from wide orbiting planet tidal-interactions (Albrecht et al., 2012; Young, A. K. et al., 2023). The foremost point is the key focus of this paper.

2.3   On the topic of disc GW Orionis

In recent years there have been detailed observations taken on warped protoplanetary discs in nature. One of particular interest is the GW Orionis system, a triple star system that displays three independent dust rings - a rare circumtriple disc (Kraus et al., 2020; Bi et al., 2020; Czekala et al., 2017). GW Orionis hosts a central binary-star pair, GW A and GW B, with a tertiary
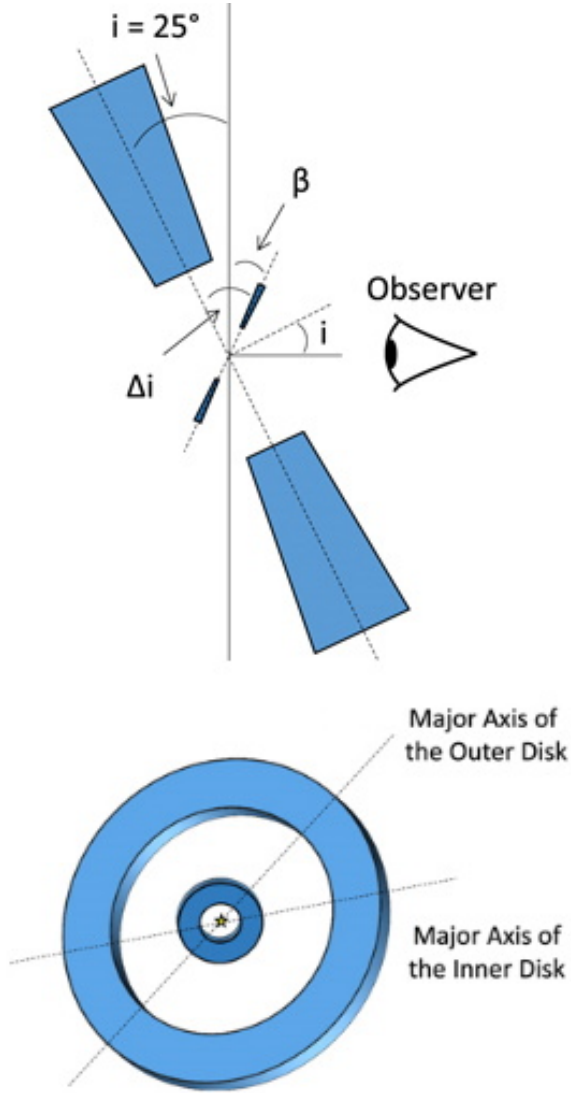
Figure 2: A visual representation of the geometry of a misaligned inner disc, taken from Long et al. (2017). The top represents the disc from a side-on view, displaying the outer and inner discs in blue. β is defined as the inclination of the inner disc from face-on, i is the face-on positive inclination of the outer-disc with respect to the observer, then $\Delta i = i - \beta$ is their difference. The bottom presents a simplified graphic of a disc's structure from a face-on view. Neither of these were made to scale.

star GW C (Berger, J.-P. et al., 2011). An artist's interpretation of this can be seen in Figure 3, an observed image in Figure 4 and then a three-dimensional graphic in Figure 5. The outermost ring is the largest dust ring observed in a protoplanetary disc, and its innermost disc is highly eccentric, causing partial obscuration of the central A-B binary pair. Analysis of GW Orionis' Spectral Energy Distributions (SEDs) showed that the inner dust rings undergo major readjustment on an ≈ 20 year time-scale.

There are a handful of suspected reasons for its misalignment; one is that it arose due to instability in the clouds that formed its respective stars. Another proposed explanation is that after binary formation, accretion of cloud material had misaligned angular momentum with respect to the host binary. A third hypothesis is that its triple stars can be modelled as an AB-C pair, and an increase in their eccentricity may arise due to resonant interactions with the binary (Papaloizou, J. C. B. et al., 2001). These resonant interactions remove angular momentum from the inner disc, but since the total energy remains constant the AB-C's orbit is unable to remain circular.

Simulations of GW Orionis have been computed; one showed no break between the inner and middle rings, instead it produced a global warp. This implies that the misalignment is caused by a different mechanism; one hypothesis is that a super-Earth companion causes the break. If the disc ends up in the viscous regime, then breaking from torque is possible - but observations suggest this is not the case. Another simulation found the disc to break into multiple recognisable planes. One closely re-
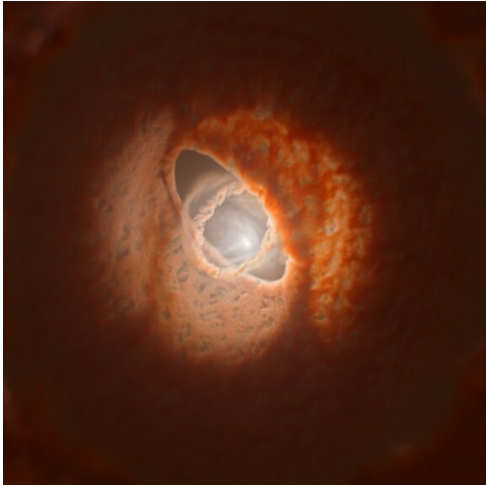
3

Figure 3: Artist's interpretation of GW Orionis, taken from the ESO (Information@eso.org, n.d.). Here its misaligned inner disc about its central stars can be clearly viewed, along with its outer disc region.
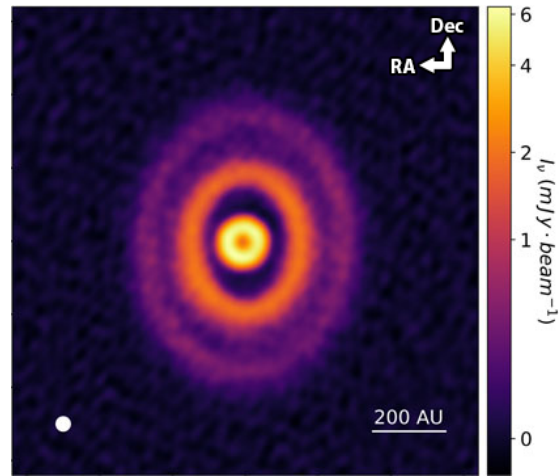

Figure 4: Taken by ALMA, this is a self-calibrated 1.3mm dust continuum map, centred on GW Orionis, with its three rings clearly visible (Bi et al., 2020). The rings can be seen at approximately 46, 188 and 338 au. Their dust masses were also estimated in this study, being calculated as 74, 168 and 245 Earth masses.

sembled the innermost ring observed on GW Orionis, leading to the conclusion that this ring formed due to disc tearing. Unfortunately, this simulation did not exhibit breaking between the two outermost dust rings.

2.4 On the relevance of dipper stars

The observations of GW Orionis have been helpful in aiding our understanding of dipper stars (Ansdell et al., 2019). Dipper stars are common, making up 20-30% of young stellar populations. They have been observed to dim for short, day-long periods at a time. It is now hypothesised that they are stars within misaligned protoplanetary discs, and these dimmings are caused by various mechanisms. The primary four mechanisms are: accretion-driven disc warps, vertical disc instability, dusty disc winds, and a broken inner disc. The last mechanism is observed in GW Orionis, as previously stated; GW Oironis' broken inner disc causes obscuration of its host binary, leading to a dimming effect. Simplistic visualisations of these mechanisms can be seen in Figure 6.

2.5 Additional observations

Two relevant observations are those of the discs HD100453 and HD143006 (Benisty, Stolker, et al., 2016; Benisty, Juhász, et al., 2018); images of these disc are astoundingly similar to disc images produced in simulations. Both discs were observed to display
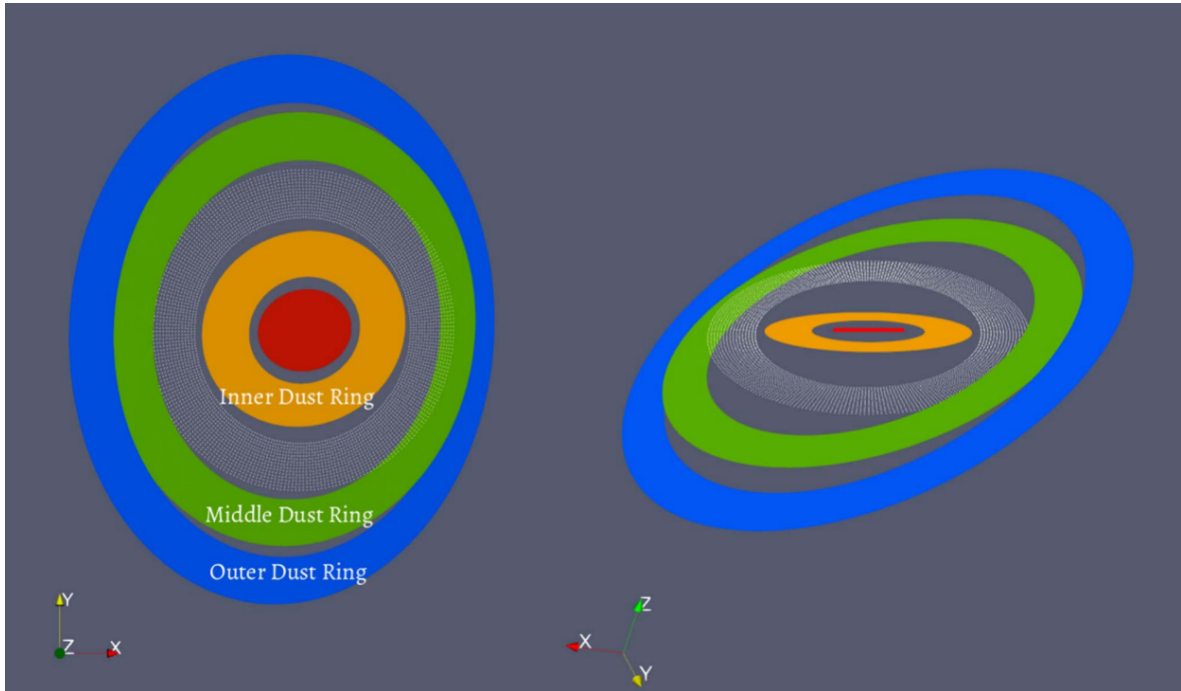
Figure 5: A three-dimensional (not-to-scale) graphic that displays the suspected orientation of GW Orionis; its three rings and their misalignment are visualised and the orbital planes of AB-C binary are shown in red. The x-axis is defined as being anti-parallel to the R.A. direction, the y-axis parallel to the Dec. direction, and z pointing towards the direction of observation. Figure taken from Bi et al. (2020).

asymmetry, a prominent cavity, rings, gaps, and multiple spiral arms; these can all be inferred as evidence for misalignment. The origin of their spiral arms is yet to be theorised, and further research is needed on the matter. A labelled polarized intensity image of HD143006 can be seen in Figure 8, and one of HD100453 in Figure 7.

2.6   On the subject of disc shadowing

As of 2017, $\approx 21\%$ of all published images of transitional discs displayed shadowing (Long et al., 2017); their exact origins are currently under debate. Three causes

for the dark features in HD 100453 were proposed:

- A physical gap from the clearing of a large body

- Grain and growth settling

- A misaligned inner disc component

The foremost reason was dispelled, as the cavity's size needed an M-type companion to be present, which was not observed. On grain growth, Birnstiel et al. (2012) found grain growth to be responsible for lowering disc's SED amplitudes, but the dimming effects were not significant enough to match with observations.
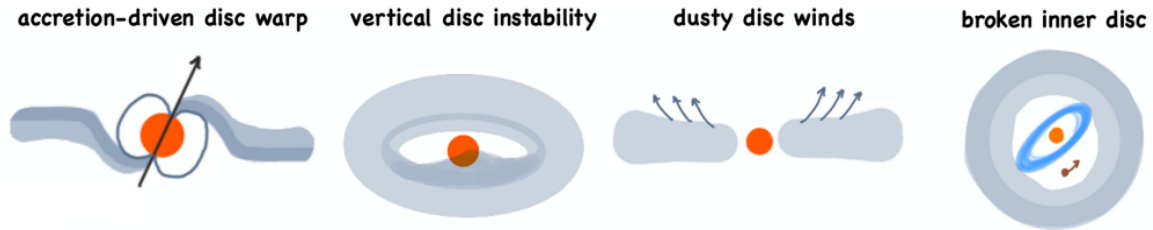
Figure 6: The suspected four primary mechanisms responsible for dipper stars, taken from Ansdell et al. (2019). The first mechanism, accretion-driven disc warping, is when the inner disc edge accretes onto the star, partially obscuring the star while the disc rotates. Vertical disc instability is when instability in the disc creates vertical structures that can obscure the star. Dusty disc winds are when dust clouds lifted by disc winds cross our line of sight with the star. The last mechanism is when a protoplanetary disc's broken inner disc causes concealment of the host star.

Inner discs misaligned by even less than a degree can cast non-axisymmetric shadows extending across their outer discs (Nealon et al., 2019; Bohn et al., 2022). Thus the study of outer disc shadows is a helpful tool for probing misaligned inner discs' geometries and thicknesses (Min, M. et al., 2017). Hence, a bridge could be formed between interferometric inner disc observations and outer disc images via the study of their shadows. The shadows are hypothesised to move with the inner disc's precession rate, and observations on the TW Hydrae disc show shadows to display strong azimuthal variations (Debes et al., 2017; Poteet et al., 2018; Teague et al., 2022).

Simulations performed by Nealon et al. (2019) supported the disc misalignment hypothesis, but argued that it is unlikely to be the cause of TW Hydrae's arrangement, due to difficulty sustaining the configuration across observationally possible time frames. This research led to the hypothesis that shadowing effects in TW Hydrae could arise from a misaligned planet in the outer disc; from a misaligned stellar magnetic field warping the inner disc; a misaligned inner planet at $\approx$ 5 au; or finally from multiple planets driving precession.

3   Method

3.1   PHANTOM

Simulations in this field are mostly done with the Smoothed Particle Hydrodynamics (SPH) code PHANTOM; which computed all simulations here. SPH is a computational method, originally developed in 1977, that carries out fluid simulations in an astrophysical context (Gingold and Monaghan, 1977). SPH works by solving the Lagrangian form of the equations of hydrodynamics. PHANTOM is a recent SPH code developed over the past decade, used primarily for the simulation of stellar, galactic, planetary, and high energy astrophysics (Price et al., 2018). PHANTOM has been used in a multitude of astrophysical research areas, from star cluster formation to
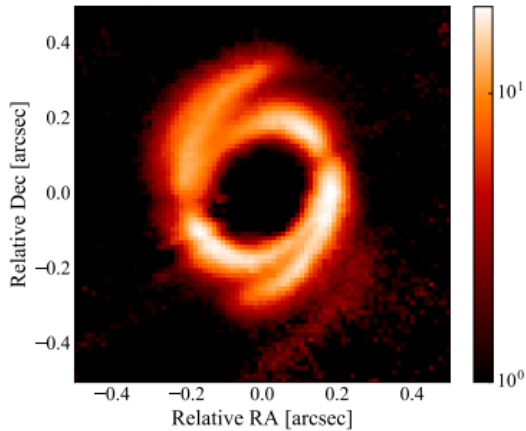
Figure 7: A polarized intensity image of HD100453, scaled by r^2, which accounts for the r^{-2} dependency of stellar lumination, taken from Benisty, Stolker, et al. (2016). Spiralling is clear, which implies warping.
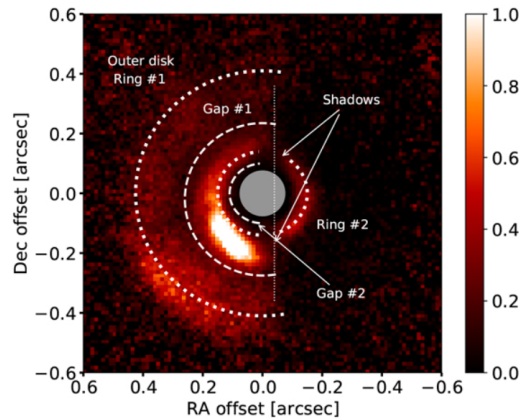

Figure 8: A labelled polarized intensity image of HD143006, scaled by r^2. The most important features indicative of misalignment are labelled - these are its shadows, gaps and rings. Obtained from Benisty, Juhász, et al. (2018).

cosmological simulations. It is notable for being more efficient at computing higher resolutions than older SPH codes (Lodato and Price, 2010).

PHANTOM uses two types of particles in its simulations - *SPH particles* and *sink particles*. Standard SPH particles represent gas in simulations, and make up the majority of simulated particles. It can also include dust particles of varying sizes, which can couple to gas particles via drag forces. There are two implementations of this - one-fluid and two-fluid algorithms. The former algorithm models the dust and gas together using a single particle for both; the latter models dust and gas with two separate particles. Sink particles, on the other hand, represent point masses, such as stars or planets (Bate et al., 1995).

3.2   SPLASH

SPLASH is an SPH visualisation software utilised extensively in viewing PHANTOM simulation files (Price, 2007); SPLASH is unique as it is designed specifically for SPH visualisation. The software is intuitive, allows visualisation in a choice of one, two or three dimensions, and can work both interactively and non-interactively. An example of an interactive SPLASH image is provided in Figure 9. The primary use of SPLASH was to make inspections of PHANTOM disc images.

3.3   MCFOST

MCFOST is used to generate scattered light images of PHANTOM simulations. MCFOST is a continuum 3D radiative transfer code, which uses the Monte-Carlo method (Pinte, Ménard, et al., 2006; Pinte, Harries, et al., 2009). PYMCFOST was also made use of,
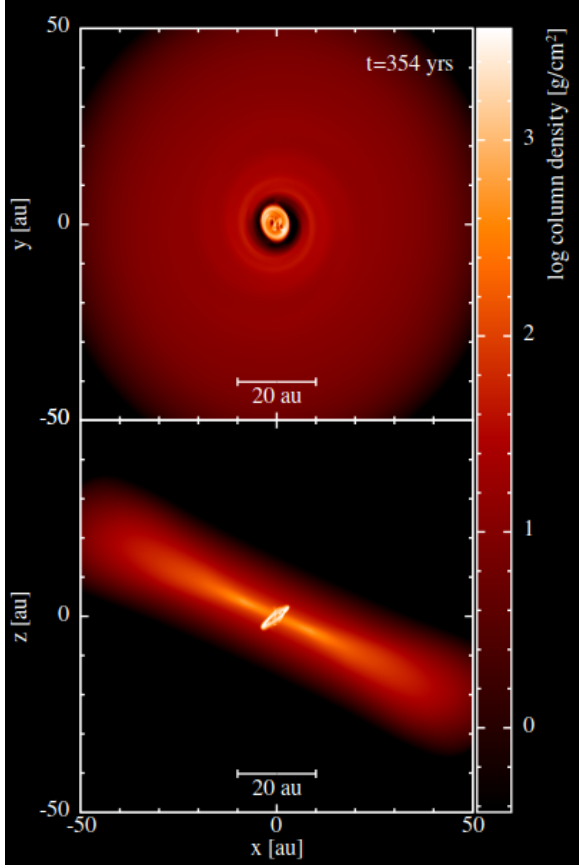
which is a python interface for MCFOST[1]. MCFOST is utilised to create scattered light images and extract properties of PHANTOM disc simulations. The following section provides an overview of how MCFOST's numerical code works.

3.3.1 How MCFOST generates scattered light images

MCFOST uses a spatial grid, defined in cylindrical coordinates, made up of N_r logarithmically-spaced radial grid cells and N_z linearly-spaced vertical grid cells, the quantities held constant in each. Within each cell, an independent dust population is contained. The dust grains are considered to be spherical and homogeneous, as per the Mie theory (Mie, 1908). The extinction and scattering opacities are calculated via the following equation:

$$K^{ext/sca}(\lambda, \mathbf{r}) = \int_{a_{min}}^{a_{max}} \pi a^2 Q_{ext/sca}(\lambda, a) f(a, \mathbf{r}) da$$

(1)

Where $f(a, \mathbf{r})$ is the composition distributions, $K^{ext/sca}$ is the opacities, and $Q_{ext/sca}(\lambda, a)$ are the scattering and extinction cross sections of a dust grain at wavelength λ of size a.

Circumstellar-dust thermal emission and photospheric emission are the two radiation sources which MCFOST deals with. The distance between interactions is calculated in MCFOST by means of optical depth, instead of via physical distances. The position of interaction $\mathbf{r}$ is computed with the method following. In an area of interaction, the optical depth τ is chosen

Figure 9: Two SPLASH log column density plots of a disc with a highly eccentric ($e = 0.8$) host binary pair, ≈ 354 years old. The top image is in the x-y plane, the misaligned inner disc clearly visible in the centre. The bottom image is in the x-z plane, displaying a slice through the disc centre. Warps and misalignments can be easily discerned in this plane. These plots are highly-interactive: the scale can be converted from non-logarithmic to logarithmic; the images can be zoomed in and out; the scale limits can be adjusted by clicking the scale bar, etc.

---

[1]https://github.com/cpinte/pymcfost

randomly with the probability distribution $p(\tau) = exp(-\tau)$. The distance l is obtained from the infinitesimal optical depth $K^{ext}(\lambda, \mathbf{r})\rho(\mathbf{r})$, which is integrated until the equality below holds true:

$$\tau_\lambda = \int_0^l K^{ext}(\lambda, \mathbf{r})\rho(\mathbf{r})ds \qquad (2)$$

The probability that the event is a scattering event rather than an absorption event is estimated using the local albedo:

$$\mathcal{A}(\lambda, \mathbf{r}) = \frac{\int_{a_{min}}^{a_{max}} \pi a^2 Q_{sca}(\lambda, a)f(a, \mathbf{r})da}{\int_{a_{min}}^{a_{max}} \pi a^2 Q_{ext}(\lambda, a)f(a, \mathbf{r})da} \qquad (3)$$

Where $\mathcal{A}(\lambda, \mathbf{r}) = p_{sca}$.

MCFOST also uses the Stokes formalism to compute both linear and circular polarisations. A light packet's state is given by its Stokes vector, and the interaction of a dust particle with a photon is described by the Mueller Matrix, $\mathbf{S}$, a 4x4 matrix. This matrix is defined in two separate ways - one Mueller matrix per grain size, or one mean Mueller matrix per grid cell. These two methods are essentially the same, so can be used interchangeably.

3.3.2   Temperature calculations

Another use of MCFOST is in calculating the temperature, which was found for every single PHANTOM simulated disc. MCFOST assumes radiative equilibrium about the entire model's volume, and assumes the dust opacities are independent of temperature. Two opposite assumptions are applied by MCFOST when making temperature calculations. It assumes no thermal coupling between gas and dust, and gives each grain

size a unique temperature, or it assumes the gas and dust are in perfect local thermal equilibrium (LTE). LTE makes the opposite assumption, assigning all dust grains and gas particles equal temperatures. In LTE, the cell temperature is calculated using the radiative equilibrium equation:

$$4\pi \int_0^{\inf} K_i^{abs}(\lambda)B_\lambda(T_i)d\lambda = \Gamma_i^{abs} \qquad (4)$$

We define Γ_i^{abs} as the energy absorption rate and B_λ as the spectral radiance for wavelength λ at temperature T (Chandrasekhar, 1960). When, instead, there is no thermal coupling between dust and gas particles each grain size has a unique temperature, thus the radiative equilibrium temperature must be done independently for each grain of size a in cell i:

$$4\pi \int_0^{\inf} K_i^{abs}(\lambda, a)B_\lambda(T_i(a))d\lambda = \Gamma_i^{abs}(a) \qquad (5)$$

This is resource-intensive, so MCFOST pretabulates temperatures at $N_T = 1000$ logarithmically spaced temperatures and then interpolates between these to obtain final temperatures for each cell.

3.3.3   MCFOST **SED calculations**

An important MCFOST output is the SED, from which the luminosity can be calculated. MCFOST uses various methods to set the energy of a photon packet and calculate the SED, which improves its efficiency. Packet energies and their number of photons are optimised depending on the calculation's aims. Both the temperatures and

SEDs are calculated with the following process:

Step one - the temperature is determined. Photon packets are generated and calculated until they leave the medium. Bjorkman and Wood (2001) formulated two concepts which have been introduced into MCFOST - *immediate reemission* and the *temperature correction method*. These improve the efficiency of calculating the re-emission process, making it so when a packet is absorbed, it is re-emitted instantly, and its wavelength is chosen by accounting for the temperature correction with the probability distribution below:

$$p_\lambda d\lambda \propto K_i^{abs}(\lambda) \left(\frac{dB_\lambda}{dT}\right)_{T_i} d\lambda \qquad (6)$$

Here, all photon packets have the same luminosity and are randomly scattered/absorbed within the disc. Another concept, *mean intensity*, proposed by Lucy (1999) is then used to reduce noise in the temperature estimations.

Step two - the final temperature calculations completed prior are utilised to compute the SED. The number of photon packets is held constant at every wavelength and only scattering of photons is allowed - no absorption. To account for the energy that will have been removed from absorption, the Stokes vector is weighted by the scattering probability, p_{sca}. The luminosity of the emitted $N_{\gamma step2}$ packets at a wavelength λ is given by the total energy that the disc and star radiates at the wavelength, calculated by the equation:

$$\epsilon_\lambda = \frac{L_*(\lambda) + \Sigma_i \omega_i(\lambda) L_i(\lambda)}{N_{\gamma step2}} \qquad (7)$$

In order to define ω_i, the "dark zone" must be explained. This "dark zone" is defined in order to avoid generating photons that are in areas of optical thickness so high that none would escape with any remaining energy. This is defined as all cells where the optical thickness is at least $\tau_\lambda = 30$ in any direction, up to the computational grid's boundary. Thus, a weight ω_i is introduced and any photons in this "dark zone" have their emission probability set to 0 from fixing $\omega_i = 0$. For cells outside of this zone, we simply set $\omega_i = 1$.

3.3.4 MCFOST **example outputs**

An example of a MCFOST SED plot can be seen in Figure 10. The SEDs x-axis is the wavelength in microns, the y-axis is the flux-density in watts-per-square-metre. This is calculated via the process outlined above.

Figure 11 shows a MCFOST scattered light image plot. An important MCFOST input parameter is the wavelength. This was usually a low-wavelength, infrared value of 1.6 microns, based on James Webb Space Telescope's viewing range of 0.6 to 28.5 microns[2] and will produce an image similar to what may be observed by telescopes. High-wavelength infrared images of 1000 microns were also produced, providing a clear view of the disc's structure. An example of a high-wavelength infrared image can be seen in Figure 12. The number of photon packets in an image can also be altered. This value is usually set to 1×10^8, but higher values such as 5×10^8 are viable and can reduce noise in output images.
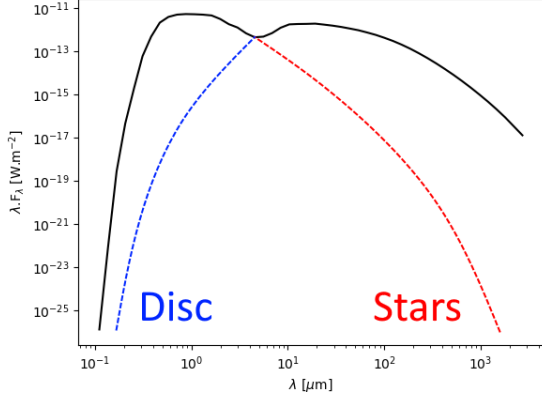
---

[2]Obtained from jwst.nasa.gov

Figure 10: An example of a MCFOST SED output, taken from a circumbinary disc with a host binary eccentricity of 0.4, $\approx$ 142 years old. In all obtained SEDs, two defined peaks can be seen. One from the host-binary stars, the second from the outer disc. Note the red and blue lines have been over-plotted, and are not present in the original SED.

3.4   Luminosity analysis

The total luminosity of a disc can be calculated with the SED via the following method. Firstly, the wavelengths are converted from microns to metres, then the flux-densities converted to specific fluxes by dividing the flux-densities by the wavelength. The python package SCIPY then integrates over both the specific fluxes and wavelengths, obtaining a total flux for the entire system using Equation 8. With this, Equation 9 is used to obtain the total Luminosity.

$$f = \int_{\lambda_i}^{\lambda_f} f_\lambda d\lambda \qquad (8)$$

$$L = 4\pi d^2 f \qquad (9)$$

Where we define f as the total flux (Wm^{-2}), f_λ as the flux per wavelength (Wm^{-3}), λ as the wavelength (m), λ_i and λ_f as the initial and final wavelengths respectively, then L as the total luminosity (W) and d as the Earth-object distance (au).

The luminosity can be analysed from visual inspection of an SED. From an SED, the flux in Wm^{-2} can be obtained from taking measurements along the y-axis. The flux here is directly proportional to the total luminosity, so the SED provides an indication of where changes in total luminosity are coming from - the host binary or the outer disc.

3.5   Shadow Analysis

3.5.1   Shadow sizes

Relative discs' shadow sizes were analysed, which is useful in determining if the shadows play a role in the disc's evolution. The MCFOST scattered light images were imported into a photo-editing software, where the shadows were outlined and the shadow area (in pixels) output, the disc's total area was computed in the same manner. The shadow area is then divided by the total disc area, producing a percentage of disc covered by shadow. This was done for all $0°$ images, the most face-on images and thus the most accurate representation of the relative shadow sizes.

3.5.2   Shadow angles

The angle between disc shadows was also computed. Min, M. et al. (2017) found the angle between shadows in the outer disc's plane to be:
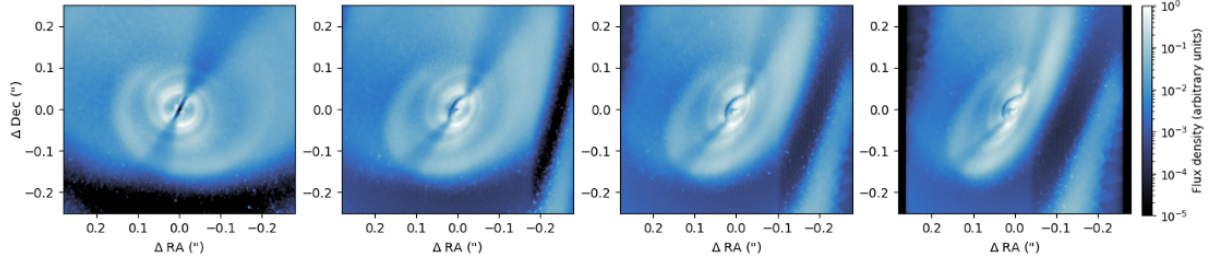
Figure 11: An example of a MCFOST scattered light image, showing an ≈ 200 years old circumbinary disc with an eccentric host binary, with $e = 0.8$, 5×10^8 photon packets, taken at 1.6 microns and displayed at 4 inclinations - $0°$, $20°$, $40°$ and $60°$ (from left to right).
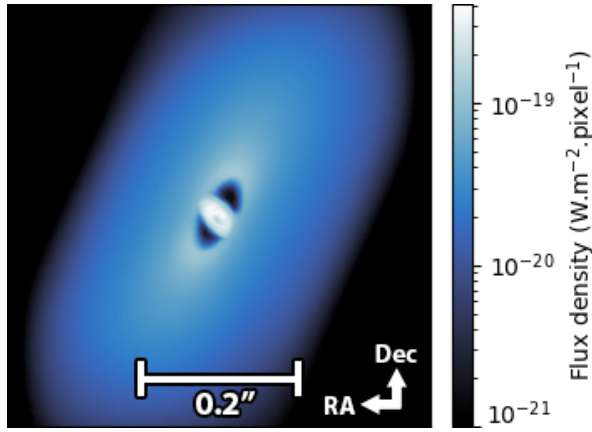

Figure 12: A 1000 micron image of the same disc in Figure 11, at the $60°$ viewing inclination. The prominent features of warping such as spirals and shadows cannot be seen here - however, the overall shape of the inner and outer disc is clearer than in 1.6 micron images, making it a useful tool for seeing a disc's geometry. $0.2" \approx 28$ au.

$$\omega = 2tan^{-1}\left(\frac{tan^2(\Delta\theta)}{(h/R)^2} - 1\right)^{1/2} \quad (10)$$

Where ω is the shadow angle, $\Delta\theta$ is the misalignment of the two discs, h is the shadow height on the scattering surface of the outer disc, measured from the mid-plane in au, and R is the radius at which the shadow begins in au.

In a MCFOST scattered light image, the shadow's starting coordinates (RA, Dec) are taken in arcseconds, and its magnitude measured via:

$$R(") = \sqrt{RA(")^2 + Dec(")^2} \quad (11)$$

Which provided R in arcseconds. This was then converted into radians, and multiplied by the distance from observer (defined as 140 Mpc for all simulations) to obtain R in parsecs. This is then simply converted into au (1 pc = 206265 au) to provide a final value for R. Figure 13 shows a visual representation of where R is approximately measured at for all discs.

To obtain h, the height of the scattering surface must be determined. This is defined as the height in the disc where the radiation hits an optical depth of $\tau = 1$, which can be computed with MCFOST when producing scattered light images. This outputs the (x, y, z) coordinates of the $\tau = 1$ surface for each pixel. The midplane is calculated via a coordinate transform between a warped and normal coordinate system. The first step to

12

obtaining the midplane height is to obtain the position vectors of the warped disc midplane, done by rotating the x-y plane by the tilt and twist, as shown:

$$R_{m.p.} = (x', y', z') = Y(\beta)Z(\gamma)(x, y, 0) \tag{12}$$

Where $Y(\beta)$ and $Z(\gamma)$ are defined as the rotation matrices for rotations of β and γ, and $R_{m.p}$ is the position vector of the warp midplane. Thus, the z-midplane is determined to be simply $z_{m.p} = 0 - z'$. Following on from this, h can then be obtained as the difference in the midplane and the $\tau = 1$ surface at the coordinate where R was measured.

The final variable needed is the disc misalignment, $\Delta\theta$. This is obtained from inspection of the tilt, β. It is simply the difference in tilt between the inner and outer discs, an example of this can be seen in Figure 15.

With all these values acquired, Equation 10 is used to obtain the angle between shadows as measured on the outer disc. It should be noted that this equation was not originally used for discs without eccentric binary host stars, so there is no prior research available as to whether or not this equation holds true in the eccentric circumbinary scenario, which it will be applied to here.

Aside from calculating the angle ω, it was also approximated from visual inspection of the shadows in an image editing software. This allowed for double checking the calculated results and ensuring their plausibility. For all discs, two angle measurements were made: one for the angle between the middle of the shadows; one for the angle between the nearest edges of the shadows. An example of these measurements being made is shown in Figure 14.

4   Results

In the following section we present the results of how varying the eccentricity of a protoplanetary disc's binary host star can alter its structure. The key ways in which these changes will be inspected are from looking at a disc's warp amplitude - Ψ, tilt - $\beta(R,t)$ and their twist - $\gamma(R,t)$ (Young, A. K. et al., 2023). The warp amplitude is a measure of how distorted a disc is at a specific radius:

$$\Psi = R\left|\frac{\partial l}{\partial R}\right| \tag{13}$$

We define $l(R,t)$ as the unit angular momentum vector of the gas averaged in a ring within the disc. The tilt, $\beta(R,t)$, is the misalignment of a cylindrical ring of radius R within the disc with respect to the binary and disc's total angular momentum vector. The twist, $\gamma(R,t)$, is the disc's transformation in the azimuthal direction; visual inspection of the disc's evolution was also performed via SPLASH and MCFOST.

Three discs varying in their host binary eccentricity are the primary focus of this paper. Their constant parameters were their inner radius $R_{in} = 2.5$ au, an outer disc boundary of $R_{out} = 50$ au, central star masses of $M = 2M_\odot$, a disc mass of $M_{disc} = 0.010M_\odot$ and an initial disc inclination of $i = 25°$. Each disc's host binary has an eccentricity of $e = 0.4$, $e = 0.6$ and finally $e = 0.8$; the third and most eccentric disc became the primary focus.
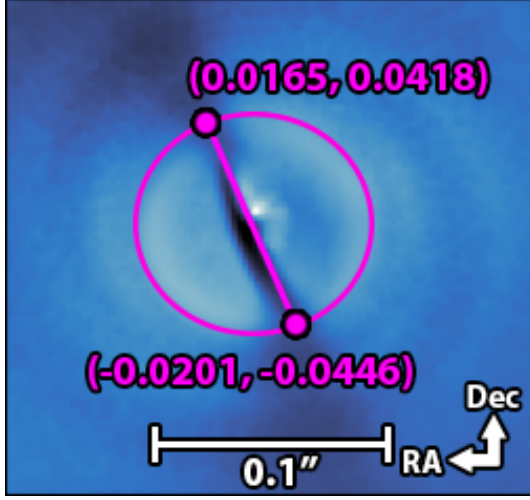
Figure 13: Zoomed in MCFOST generated scattered light image displaying approximately where R is measured for two opposing shadows; the (RA, Dec) coordinates in arcseconds are overplotted. 0.1" $\approx$ 14 au.
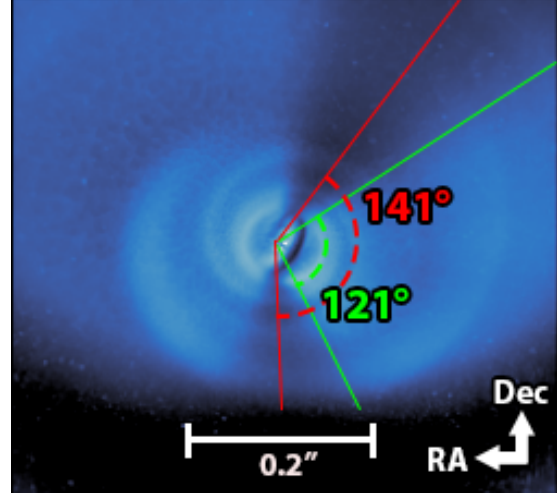

Figure 14: Visual approximation of the angle between shadows, done in the face-on ($i = 0$) image for every measurement. In red - the angle measured from the middle of the shadows, in green - the angle measured from the nearest shadow edges. 0.2" $\approx$ 28 au.

4.1 General observed trends of warped discs

Before focusing exclusively on eccentric circumbinary discs, circumbinaries that varied solely in their inclination were analysed. This was useful in understanding general trends circumbinary discs follow without eccentric host stars. Four discs were used, all with a binary mass ratio of $\mu = m_2/(m_1 + m_2) = 0.3$ and initial misalignments of $40°$, $60°$, $120°$ and $150°$. Images of these discs 212 years after their simulation start[3] are shown in Figure 16. The $40°$ disc displayed a smooth warp, but was stable overall. The $60°$ disc produced a misaligned and detached inner disc, while its outer disc maintained minimal warping. The $120°$ disc exhibited minor outer disc warping, then a well defined, highly-circular and slightly misaligned inner disc. The $150°$ disc had the most prominent misaligned and detached inner disc, but likewise displayed minimal outer disc warping. From this information, it can be inferred that retrograde discs develop misaligned inner discs more commonly than prograde discs.

4.2 Age conversion

Before presenting results, a moment will be taken to define the conversion of the timestamps which will be used henceforth. Disc ages are defined by a timestamp, where a value of 1000 corresponds to 444.3 definable time units, 1 of which is equal to 5.023×10^6
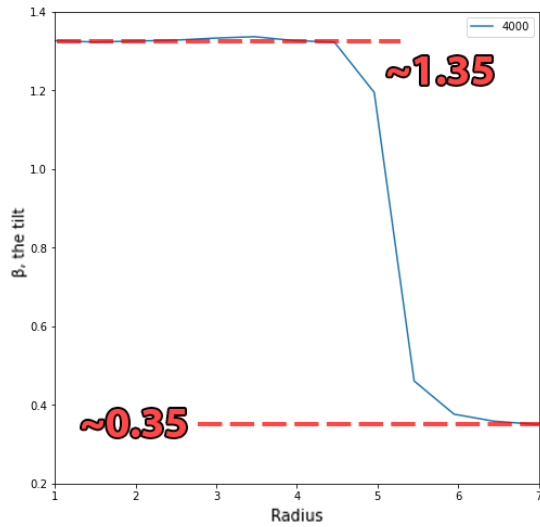
---

[3]The simulation start signifies a protoplanetary disc $\approx$ 1 Myr old.

Figure 15: $\Delta\theta$ is obtained from plotting the tilt β and measuring the difference in the tilt in the inner disc and outer disc, i.e. before ≈ 5 au and after ≈ 5 au. Here, it can be seen to drop from ≈ 1.35 to ≈ 0.35 hence $\Delta\theta = 1.35 - 0.35 = 1$ in radians.

seconds. The approximate conversion to be used hereafter is a timestamp difference of 100 being equated to ≈ 7.09 years. An example - a disc with a 2000 timestamp will be $20 * 7.09 \approx 142$ years old since the model initialisation. The model begins at the 0 timestamp, signifying a disc with an ≈ 1 Myr old structure.

4.3   On warp amplitudes

All three discs showed evidence for warping. Warp amplitudes were calculated and graphed, as seen in Figure 17. Warp amplitude can be indicative of disc breaks, which are inferred by a prominent spike in the amplitude. This is clearly seen in the $e = 0.8$ disc, thus implying a break at ≈ 5 au. This remains for much of the disc's life, peaking

at at the 4700 timestamp, where a second, smaller peak at ≈ 2 au appears. The warp amplitude decreases after the 5000 timestamp, and is completely collapsed by 5800. An animated gif of this disc's warp amplitude's evolution was produced and uploaded to github[4].

The other two discs warp amplitudes are significantly smaller, peaking at ≈ 0.40 and at ≈ 0.7 for $e = 0.4$ and the $e = 0.6$ discs respectively, with no sharp peaks prominent. Their warp amplitudes fluctuate as radius increases, thus indicating some warping present.

4.4   On the tilt and twist

Both the tilt, β, and the twist, γ were calculated for all three discs; the tilt is plotted in Figure 18 for all three discs. As stated prior, it is a measure of the misalignment of a ring with respect to the total angular momentum of the system. From the tilt of a disc as a function of radius, the presence of a detached inner disc can be detected. The plots show the $e = 0.4$ disc to possess a steep initial tilt, which drops off sharply, then gradually increases with radius. The $e = 0.6$ disc's tilt drops off slightly at the inner radius, and then fluctuates until flattening off at the outer radius. The third disc, $e = 0.8$, has the steepest initial tilt drop off and then flattens almost completely from 5 au to the disc's outer edge. It should be noted this figure only displays the tilt up to 30 au, as past this point they remain approximately flat up to 50 au for all three.

The twist, γ, is in Figure 19 in the same

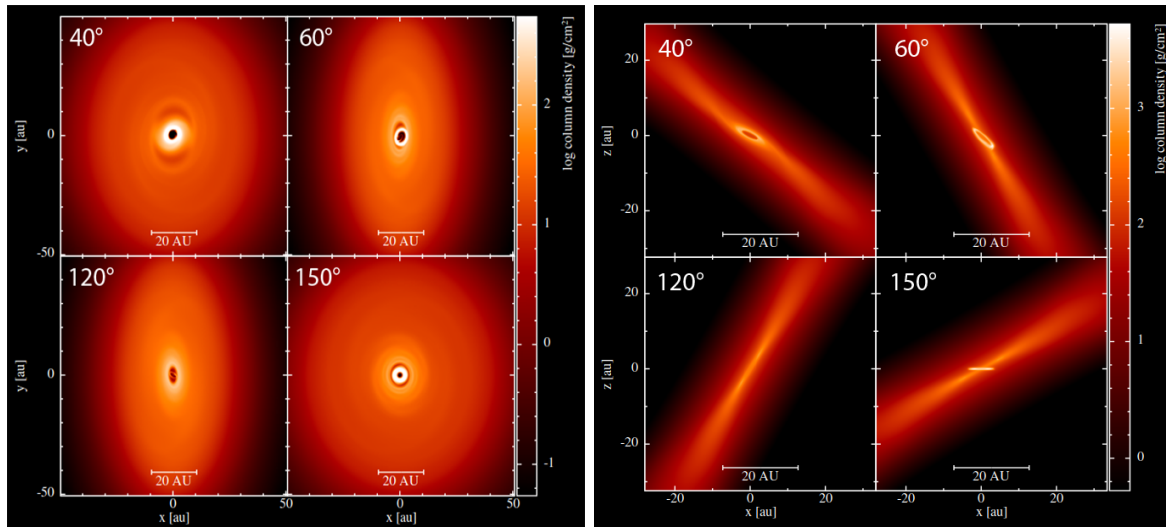[4]https://github.com/aidanjohnson42/ Senior-Honours-Project

15

Figure 16: A log-column density plot of four discs of separate initial inclinations in the x-y plane (left) and the x-z plane (right), all are $\approx$ 212 years in age. Detached inner discs can be seen in the centre, and the entire outer disc is visible in the x-y plane. In the x-z plane, the inner disc misalignment alongside outer disc warping can be seen clearly.

format used prior. The x-axis only extends to 15 au, as past this point twist remains approximately flat until 50 au. As stated prior, the twist is the disc's transformation in the azimuth, as a function of radius. The two lower eccentricity discs display twists that are almost directly proportional to the radius, which continues all the way to the disc's outer edge. The highest eccentricity disc's twist is initially level, then spikes at 5 au and remains relatively level throughout the remainder of the disc. This is not the case for the 6000 plot, which is essentially flat throughout.

4.5   Luminosity variations

Total luminosities were calculated for the $e = 0.8$ disc at 35 timestamps in total - 1980 to 6900 (140 years to 489 years). The total luminosities as a function of time are plot-

ted in Figure 20. The flux amplitudes for this disc and its host binary were also obtained for 33 timestamps (discounting the 6000 and 6900 timestamps, as by this point the system's total luminosity had begun to tail off) which can be seen in Figure 22. Separate SED amplitudes were plotted to discern a relationship between total luminosity and individual disc and star luminosities.

4.6   Shadow Results

4.6.1   Shadow sizes

The relative shadow size for the $e = 0.8$ disc was calculated for 31 timestamps, from 1980 to 5000. Figure 21 shows a plot of the relative shadow size as a function of time time. The 3300 and 3400 shadow sizes were not calculated, as in these the discs appeared entirely shadowed.
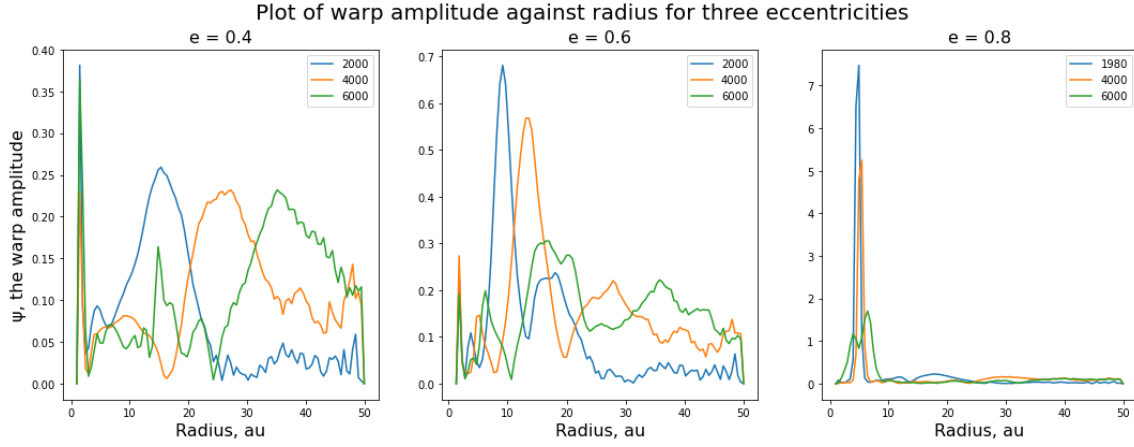
Figure 17: Comparison of warp amplitude against radius for discs with varying eccentricities. A large, defined peak implies breaking at its respective radius, as seen in the $e = 0.8$ plot. The two other plots have much smaller warp amplitudes, hence implying no breaking.

4.6.2 Shadow angles

The shadow angles were calculated at two separate radii for both opposing shadows in five discs. The results for this can be seen in Table 1, along with the visually obtained angles.

5 Discussion and Analysis

In the section following, the results for all three discs will be discussed in turn. Then, the luminosity variations, the size and angles of the shadows in the high-eccentricity $e = 0.8$ circumbinary disc will be discussed.

5.1 On the tilt, twist and warp amplitudes

Here, the results presented prior on the tilt, twist and warp amplitudes of all three discs will be discussed sequentially.

5.1.1 The e = 0.4 disc

The $e = 0.4$ disc was the lowest eccentricity disc analysed here, and exhibited the least amount of warping. Its warp amplitude peaked at 0.40 in the 6000 timestamp, but generally did not go higher than ≈ 0.25. As noted prior, a detached inner disc causes a major spike in the warp amplitude. The warp amplitude dips up and down, but this is not an indication of strong warping. Minor tilting can be seen in the plots, alongside an ever so slightly increasing twist, but neither are indicative of a warp or a detached inner disc.

From these results, it can be inferred that the host star was not eccentric enough to warp the outer disc or for a detached inner disc to form. Inspection in SPLASH confirmed this result, as no warping could be seen.
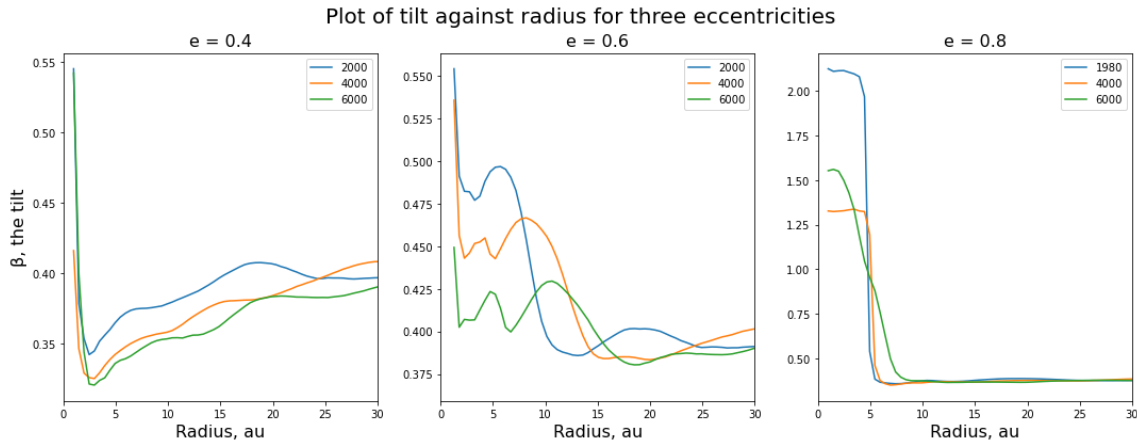
Figure 18: Tilt, β, in radians, is the misalignment of a ring with respect to the total angular momentum. From this plot of tilt against radius for discs of three eccentricities, minor tilting is seen in the lower eccentricity discs, whereas the high eccentricity has a substantially high initial tilt which quickly drops off at ≈ 5 au. Hence, a separated, misaligned inner disc ≈ 10 au in diameter can be inferred.

5.1.2   The e = 0.6 disc

The $e = 0.6$ disc is marginally more eccentric, but not eccentric enough to display significant warping or form a detached inner disc. The warp amplitude peaked at ≈ 0.7, higher than for the $e = 0.4$ disc, but its seemingly random peaks are a sign that there was no detached inner disc. The tilt goes up and down at lower radii, which could be indicative of warping. This disc was inspected in SPLASH, and in the x-z plane no warping could be seen, but the outer disc appeared messy and twisted, a feature which decreased with disc age. The twist for this disc has little variation and increases with radius, similar to the $e = 0.4$ disc, supporting the hypothesis of a detached inner disc not being present.

Thus, it can be stated that an eccentricity of 0.6 on a protoplanetary disc is still not enough to warp the outer disc significantly or to produce a detached inner disc.

5.1.3   The e = 0.8 disc

The most eccentric $e = 0.8$ host star disc has a major warp amplitude spike at ≈ 5 au, then a warp amplitude of almost 0 throughout the rest of its outer disc - a definitive indication of a detached inner disc. This spike peaks at a warp amplitude of ≈ 7 - much higher than the greatest warp amplitudes of the lower eccentricity discs. By the 6000 timestamp, this peak has shrunk considerably and also shows a second, smaller peak at a lower radius. This is an indication that by this timestamp, the detached inner disc has broken apart (or is in the process of breaking). Upon SPLASH inspection, a misaligned inner disc is clear throughout this discs lifespan, but by the 6000 time stamp has begun to lose its form. 1000 micron images were also produced via MCFOST, which show a well defined inner disc, an example of these can be seen in Figure 23.

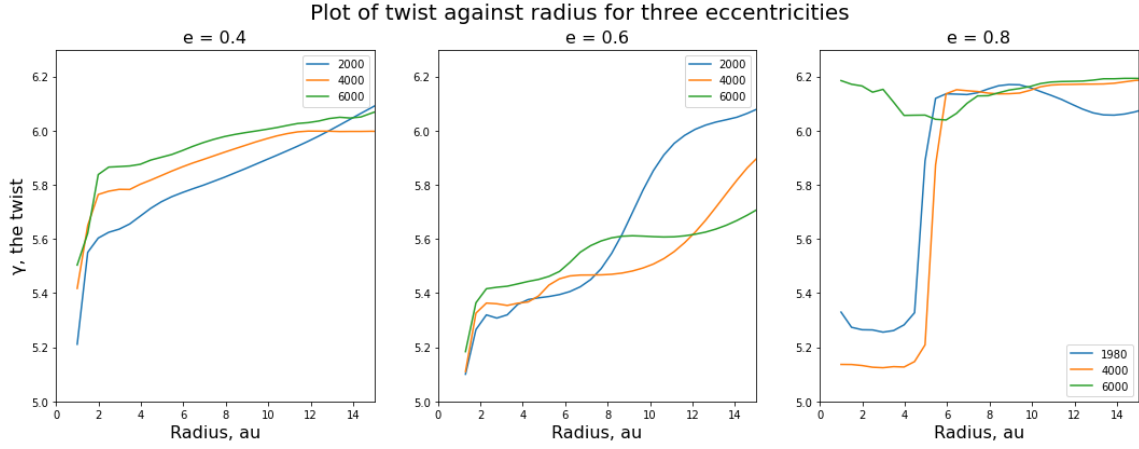The disc's tilt is flat until 5 au for the 2

Figure 19: Twist, γ, in radians, is the transformation of the disc in the azimuth. These plots show twist against radius, for three discs of varying host-binary eccentricities. The lower eccentricity discs display little variation in twist, whereas the third has a low initial twist - potentially indicative of a detached inner disc.

lower timestamps, then drops sharply and levels off at ≈ 0 for the rest of the disc's radius. The twist does the opposite - starting low and flat until 5 au, then spiking upwards and levelling off at ≈ 6.2 radians. This is not the case for the 6000 timestamp - here the tilt drops at a constant rate from the inner edge until about 10 au. At this timestamp, the twist is approximately level throughout the entire disc. Thus, both the twist and tilt are indications of a detached and misaligned inner disc, about 5 au in radius. This detached inner disc does not maintain its structure for the entire disc's lifetime, as by the 6000 timestamp it is broken completely. It should be noted this disc had the least variation in tilt, twist and warp amplitude at radii above 5 au in its outer disc, hence it can be ascertained that there is essentially no outer disc warping.

Inspection in SPLASH confirms these observations. A sizeable cavity is visible in the x-y plane, and an inner disc rotates wildly over time in all viewing planes. From these results alone, the evolution of this disc can be loosely inferred. A disc with a highly eccentric host binary quickly develops a detached and misaligned inner disc. This disc spirals constantly, eventually breaking itself apart after ≈ 425 years.

5.2 Luminosity variations in the high eccentricity disc

The variation of luminosity furthers our understanding of the disc's complete evolution. From Figure 20, the total luminosity can be seen to peak a total of five times, then trails off after the 5000 timestamp. After close inspection with both SPLASH and the MCFOST generated scattered light images, this has been attributed to the detached inner disc's misalignment.

Let us look at the largest peak at ≈ 4400 to explain this effect. At the 4000 timestamp, the inner disc is mlisaligned such that
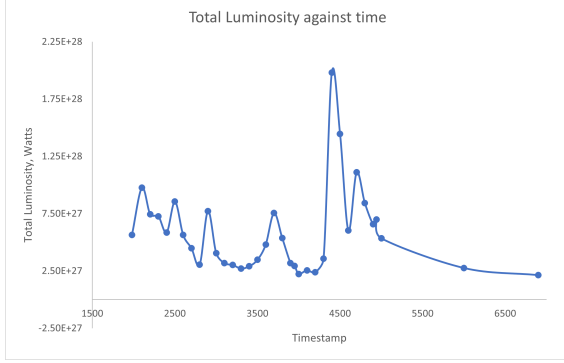
19

Figure 20: Total luminosity over time for the $e = 0.8$ disc, from the timestamps 1980 to 6900 (approximately 140 years to 489 years, a 349 year time-frame). This plot presents six definitive peaks, at the timestamps 2100, 2500, 2900, 3700, 4400 and 4700. The luminosity trails off after the last peak.
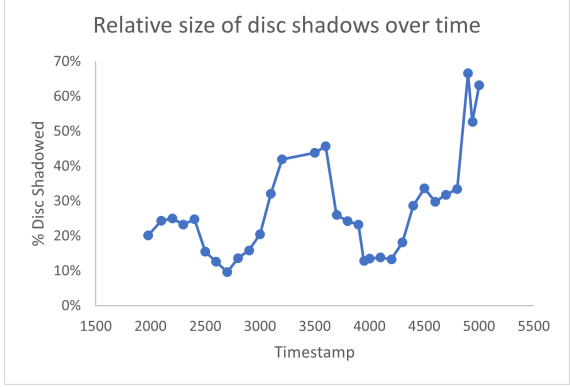
Figure 21: Relative size of disc shadows against time for the $e = 0.8$ disc. It should be mentioned that the relative shadow sizes for the 3300 and 3400 discs were not calculated, due to being almost entirely shadowed. Note the lack of correlation between shadow size and total luminosity, which will be discussed further later.

Timestamp	Shadow		(Ra, Dec) "	R (au)	h (au)	$\Delta\theta$ (rads)	ω (degs)	ω ave. (deg)	Angle estimates Mid.	Closest
2200	Left	#1	(0.040, 0.023)	6.4597	3.23590		169.27			
		#2	(0.0300, 0.0130)	4.5773	0.34240	2.10	179.78	175.70	147	132
	Right	#1	(-0.0538, -0.0123)	7.5339	2.38150		176.15			
		#2	(-0.0773, -0.0117)	10.9451	2.68230		177.60			
2300	Left	#1	(0.0329, 0.0037)	4.6350	0.08888		179.98			
		#2	(0.0557, 0.0160)	8.1133	5.02315	2.15	157.81	172.06	166	139
	Right	#1	(-0.0496, -0.0044)	6.9712	2.28821		174.47			
		#2	(-0.0733, 0.0054)	10.2897	2.89857		175.98			
2800	Left	#1	(0.011, -0.028)	4.2116	0.09425		180.00			
		#2	(0.025, -0.052)	8.0776	5.44370	1.20	171.57	176.51	175	162
	Right	#1	(-0.024, 0.039)	6.4110	2.74730		176.73			
		#2	(-0.031, 0.059)	9.3307	3.35074		177.72			
3000	Left	#1	(0.0094, -0.0385)	5.5483	1.74280		161.65			
		#2	(0.0081, -0.0573)	8.1017	4.46250	0.70	106.47	146.29	141	121
	Right	#1	(-0.0161, 0.0427)	6.3888	2.08550		159.95			
		#2	(-0.0315, 0.0615)	9.6736	3.34563		157.07			
4000	Left	#1	(0.0138, 0.0375)	5.5942	0.16540		179.96			
		#2	(0.0308, 0.0607)	9.5293	1.65230	1.00	178.56	178.48	167	119
	Right	#1	(-0.0142, -0.0389)	5.7975	0.58920		179.51			
		#2	(-0.0203, -0.0560)	8.3392	2.41907		175.88			

Table 1: The calculated shadow angles for a total of five discs, the angles estimated via image inspection are also provided.
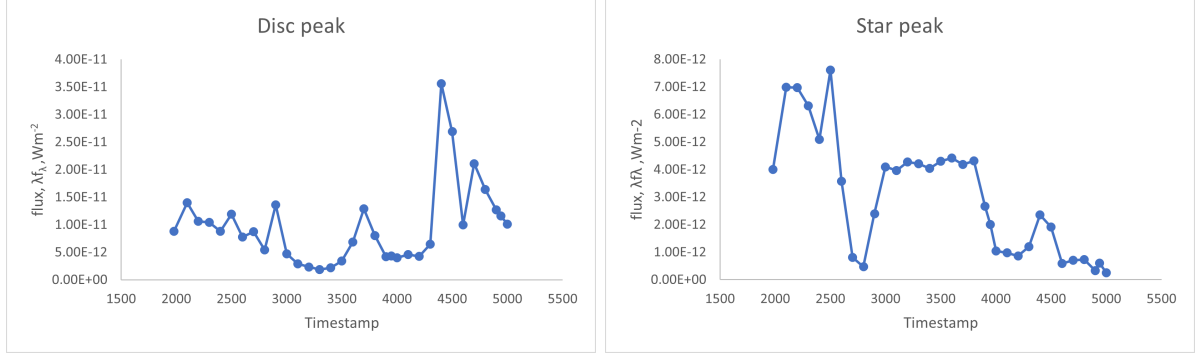
Figure 22: Plots of the $e = 0.8$ SED flux amplitudes over time for both disc peaks and the star peaks (shown prior in Figure 10). These were all taken from face on (i.e. $i = 0$). Note the difference in y-axis scales - the disc's flux amplitude is almost an order of magnitude greater than the star's. Similarities in trend between the disc's peak and the total luminosity can be spotted, which will be discussed in detail later.

it appears almost completely perpendicular to the plane of the outer disc. With this orientation, the host binary will be obscured from a face on angle, reducing the amount of light the host binary shines onto the outer disc. With time, the inner disc continues to rotate, until the 4400 timestamp where it aligns with the outer disc plane. As a consequence, the host binary now shines a great deal of light onto the outer disc, thus resulting in the observed spike in luminosity. This effect happens regularly throughout the disc's life, and is hypothesised as the primary cause for the luminosity spikes.

The two plots in Figure 22 support this hypothesis; this is due to the fact that the disc peaks when the luminosity peaks. This can be explained as the host binary's light illuminating the outer disc, therefore increasing the disc SED's flux amplitude. On the other hand, the plot of the star's flux amplitude does not correlate at all with the other two plots. The star's flux is smaller than the disc's by almost an entire order of magnitude, thus contributing little to the

total luminosity.

It should also be noted that at the later timestamps - around the same time as the peak at ≈ 4400 - the inner disc appears to undergo accretion onto the host binary. A SPLASH image of this is attached in Figure 24. This explains the subsequent disappearance of the inner disc. It could be assumed that this accretion is another cause for the luminosity spikes - however, PHANTOM does not include accretion into its calculations, so this is not possible. Of course in reality, this would not be the case, leading us to hypothesise that the latter luminosity spike would appear to be even brighter in nature.

5.3 Shadow Discussion

5.3.1 Shadow sizes

The shadow sizes varied significantly throughout the $e = 0.8$ disc's lifetime, however, these did not correlate directly with the change in total luminosity. From this it can be inferred that the size of the shad-
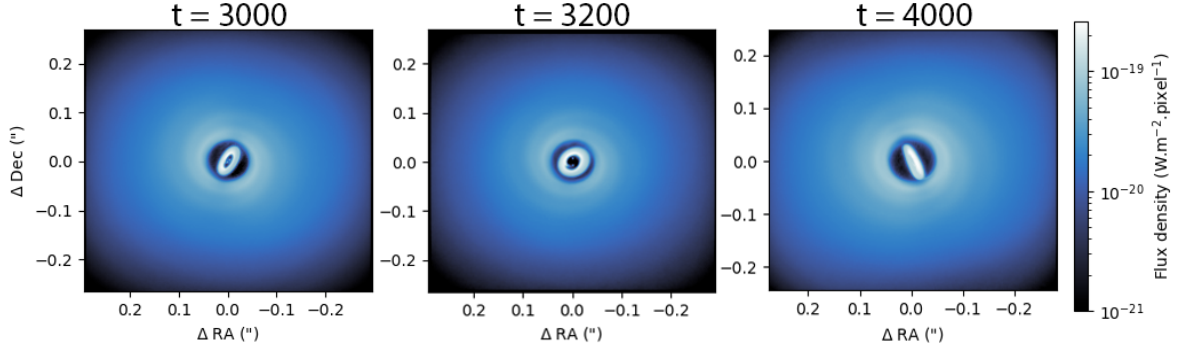
Figure 23: 1000 micron images for the $e = 0.8$ disc at three separate timestamps - 3000, 3200 and 4000. The evolution of the inner disc's orientation can be seen clearly in these images, being slightly side-ways in the first image, then flat in the plane of the outer disc in the second and finally appearing almost completely perpendicular in the third image.
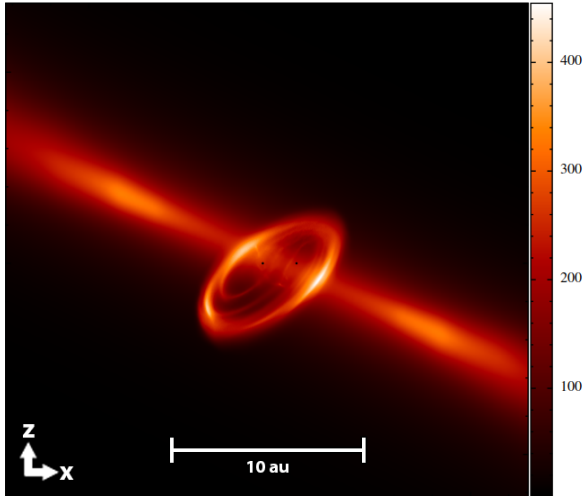

Figure 24: SPLASH image of the $e = 0.8$ disc at the 4700 timestamp. The host binary can be seen as the two central black points, and accretion into them from the misaligned inner disc is clearly visible.

ows do not directly affect the total luminosity. It should be hypothesised that these shadows are significant enough to be observed in nature, and that they provide a strong indication of a misaligned inner disc. On the other hand, they do not change on short enough time spans for the changes in shadow sizes to be observable in nature.

5.3.2 Shadow angles

The shadow angles for the timestamps 2300, 2800, 3000 and 4000 were all realistically close to their estimated angles. These were calculated as $172.06°$, $176.51°$, $146.29°$, $178.48°$ and estimated as $166°$, $175°$, $141°$ and $167°$ (from the shadow midpoints) for the 2300, 2800, 3000 and 4000 timestamps respectively. The remaining timestamp, 2200, was calculated as being $175.70°$ and estimated as $147°$. This appears to be rather distant from what it should be, but upon further inspection of the MCFOST image this could be attributed to being the angle estimation that is incorrect as opposed

to the calculation. This could be due to the disc being tilted, or the shadow's edges being blurred within the image hence making it difficult to discern the angles by eye. Another explanation for this discrepancy is that this equation has only been used before with circumbinary discs whose host binary pair are in non-eccentric circular orbits. A third explanation is that the equation is more accurate for discs with narrow shadows, the 2800 disc had the narrowest shadows and also the least discrepancy between calculated angle and estimated angle. On the other hand, the 2200 disc had the widest shadows and the largest discrepancy.

As stated earlier, no prior research has been found to show this equation work for circumbinary discs with highly eccentric host binaries. The calculated angles presented here are plausible and match up with expectations, thus this equation most-likely holds true for high-eccentricity scenarios, but further research is needed to confirm this hypothesis due to the discrepancies mentioned prior.

5.4 Could these effects be observed in reality?

If one was to look for a circumbinary disc with a highly eccentric host binary in nature, the two primary features to search for would be the shadowing and the luminosity fluctuations.

The luminosity spikes in the $e = 0.8$ disc happen at intervals of approximately 28 years, 57 years and 50 years, in turn. These are sizeable windows to look out for, but not unrealistic. To go from the 4000 timestamp to the 5000 timestamp takes roughly 71 years, but the spike itself happens decidedly quickly; going from a minimum point at 4300 to its peak at 4400 takes less than 7 years. When the luminosity increase due to accretion is taken into account, it can be hypothesised that this process could certainly be observed in a realistic time frame, and may even be significantly brighter.

Outer disc shadowing effects would also be prominent if one of these discs was to be observed, and from their alignment the geometry of the misaligned inner disc can be inferred. The size of these shadows appears to alternate with time, but not in a short timescale relative to us. The shadow angles provide a method for probing inner disc geometry, but it is unclear if they vary in timeframes short enough to be noticeable in nature.

6 Conclusion

In conclusion, it has been found from a number of simulations that high-eccentricity in a circumbinary disc's host star is a major factor in a disc's evolution and morphology. Eccentricities of 0.8 will cause a detached inner disc that becomes strongly misaligned, whereas lower eccentricities will create relatively stable circumbinary disc systems but may exhibit outer disc warping. Observation of these effects in nature could be possible, primarily via a disc's luminosity variations or the size of their shadows. In reality, they would most likely have stronger variations in their total luminosities, due to accretion which is not accounted for in PHANTOM simulations. These luminosity spikes may happen in time-frames of a few years, thus being potentially observable in nature, and are hypothesised to be a likely cause for dipper stars.

If time allowed, discs with more eccentricities would be analysed such as $e = 0.9$, $e = 0.85$, etc to gain further insight into the morphological effects of eccentricity in circumbinary discs. The shadow angles would also be computed at all used timestamps, and ideally with more measurements per shadow. This would help to gain understanding into whether the variation of shadow angles is an effect that could be noticeable in nature.

Future research could be done into what other parameters can cause warping and inner disc detachment in circumbinary discs with eccentric host stars, i.e. whether inclination or binary mass ratio could play a role in preventing or increasing their chaotic behaviour.

7 Acknowledgements

References

[1] C. R. O'dell and Z. Wen, "Postrefurbishment Mission Hubble Space Telescope Images of the Core of the Orion Nebula: Proplyds, Herbig-Haro Objects, and Measurements of a Circumstellar Disk", Astrophysical Journal **436**, 194 (1994).

[2] T. Montmerle et al., "Solar system formation and early evolution: the first 100 million years", in From suns to life: a chronological approach to the history of life on earth, edited by M. Gargaud et al. (Springer New York, New York, NY, 2006), pp. 39–95.

[3] P. J. Armitage, Astrophysics of planet formation, 1st ed. (Cambridge University Press, 2010).

[4] S. Kraus et al., "A triple-star system with a misaligned and warped circumstellar disk shaped by disk tearing", Science **369**, 1233–1238 (2020).

[5] S. M. Andrews, "Observations of protoplanetary disk structures", Annual Review of Astronomy and Astrophysics **58**, http://arxiv.org/pdf/2001.05007, 1–46 (2020).

[6] C. Walsh, T. J. Millar, and H. Nomura, "CHEMICAL PROCESSES IN PROTOPLANETARY DISKS", The Astrophysical Journal **722**, 1607–1623 (2010).

[7] L. I. Cleeves, "Zooming in on the chemistry of protoplanetary disks with alma", Proceedings of the International Astronomical Union **13**, 57–68 (2017).

[8] Lesur, Geoffroy R. J., "Systematic description of wind-driven protoplanetary discs", Astronomy and Astrophysics **650**, "A35" (2021).

[9] A. J. Winter and T. J. Haworth, The external photoevaporation of planet-forming discs, 2022.

[10] C. J. Nixon, A. R. King, and J. E. Pringle, "The final parsec problem: aligning a binary with an external accretion disc", Monthly Notices of the Royal Astronomical Society: Letters **417**, L66–L69 (2011).

[11] C. Nixon, A. King, and D. Price, "Tearing up the disc: misaligned accretion on to a binary", Monthly Notices of the Royal Astronomical Society **434**, 1946–1954 (2013).

[12] S. Albrecht et al., "Obliquities of hot jupiter host stars: evidence for tidal interactions and primordial misalignments*", The Astrophysical Journal **757**, 18 (2012).

[13] Young, A. K. et al., "On the conditions for warping and breaking protoplanetary discs", Private communication - unpublished manuscript (2023).

[14] Z. C. Long et al., "The shadow knows: using shadows to investigate the structure of the pretransitional disk of hd 100453", The Astrophysical Journal **838**, 62 (2017).

[15] J. Bi et al., "GW ori: interactions between a triple-star system and its circumtriple disk in action", The Astrophysical Journal Letters **895**, L18 (2020).

[16] I. Czekala et al., "The architecture of the gw ori young triple-star system and its disk: dynamical masses, mutual inclinations, and recurrent eclipses", The Astrophysical Journal **851**, 132 (2017).

[17]Berger, J.-P. et al., "First astronomical unit scale image of the gw orionis triple system - direct detection of a new stellar companion", Astronomy and Astrophysics **529**, L1 (2011).

[18]Information@eso.org, *The inner ring of gw orionis: model and sphere observations.*

[19]Papaloizou, J. C. B., Nelson, R. P., and Masset, F., "Orbital eccentricity growth through disc-companion tidal interaction", Astronomy and Astrophysics **366**, 263–275 (2001).

[20]M. Ansdell et al., "Are inner disc misalignments common? ALMA reveals an isotropic outer disc inclination distribution for young dipper stars", Monthly Notices of the Royal Astronomical Society **492**, 572–588 (2019).

[21]M. Benisty, T. Stolker, et al., "Shadows and spirals in the protoplanetary disk HD 100453", Astronomy and Astrophysics **597**, A42 (2016).

[22]M. Benisty, A. Juhász, et al., "Shadows and asymmetries in the T Tauri disk HD 143006: evidence for a misaligned inner disk", Astronomy and Astrophysics **619**, A171, A171 (2018).

[23]T. Birnstiel, S. M. Andrews, and B. Ercolano, "Can grain growth explain transition disks?", Astronomy and Astrophysics **544**, A79 (2012).

[24]R. Nealon et al., "Scattered light shadows in warped protoplanetary discs", Monthly Notices of the Royal Astronomical Society **484**, 4951–4962 (2019).

[25]A. J. Bohn et al., "Probing inner and outer disk misalignments in transition disks", Astronomy and Astrophysics **658**, https://www.aanda.org/articles/aa/pdf/2022/02/aa42070-21.pdf, a183 (2022).

[26]Min, M. et al., "Connecting the shadows: probing inner disk geometries using shadows in transitional disks", Astronomy and Astrophysics **604**, "L10" (2017).

[27]J. H. Debes et al., "Chasing shadows: rotation of the azimuthal asymmetry in the tw hya disk*", The Astrophysical Journal **835**, 205 (2017).

[28]C. A. Poteet et al., "Space-based coronagraphic imaging polarimetry of the tw hydrae disk: shedding new light on self-shadowing effects", The Astrophysical Journal **860**, 115 (2018).

[29]R. Teague et al., "Gas and dust shadows in the TW hydrae disk", The Astrophysical Journal **930**, 144 (2022).

[30]R. A. Gingold and J. J. Monaghan, "Smoothed particle hydrodynamics: theory and application to non-spherical stars", Monthly Notices of the Royal Astronomical Society **181**, 375–389 (1977).

[31]D. J. Price et al., "Phantom: A Smoothed Particle Hydrodynamics and Magnetohydrodynamics Code for Astrophysics", Publications of the Astronomical Society of Australia **35**, e031, e031 (2018).

[32]G. Lodato and D. J. Price, "On the diffusive propagation of warps in thin accretion discs", Monthly Notices of the Royal Astronomical Society **405**, 1212–1226 (2010).

[33] M. R. Bate, I. A. Bonnell, and N. M. Price, "Modelling accretion in protobinary systems", Monthly Notices of the Royal Astronomical Society **277**, 362–376 (1995).

[34] D. J. Price, "Splash: an interactive visualisation tool for smoothed particle hydrodynamics simulations", Publications of the Astronomical Society of Australia **24**, 159–173 (2007).

[35] C. Pinte, F. Ménard, et al., "Monte Carlo radiative transfer in protoplanetary disks", Astronomy and Astrophysics **459**, 797–804 (2006).

[36] C. Pinte, T. J. Harries, et al., "Benchmark problems for continuum radiative transfer. High optical depths, anisotropic scattering, and polarisation", Astronomy and Astrophysics **498**, 967–980 (2009).

[37] G. Mie, "Beiträge zur Optik trüber Medien, speziell kolloidaler Metallösungen", Annalen der Physik **330**, Archived english translation - Accessed 24/03/23., 377–445 (1908).

[38] S. Chandrasekhar, *Radiative transfer* (1960).

[39] J. E. Bjorkman and K. Wood, "Radiative Equilibrium and Temperature Correction in Monte Carlo Radiation Transfer", The Astrophysical Journey **554**, 615–623 (2001).

[40] L. B. Lucy, "Improved Monte Carlo techniques for the spectral synthesis of supernovae", Astronomy and Astrophysics **345**, 211–220 (1999).